

Capacitive coupling induced Kondo-Fano interference in side-coupled double quantum dots

Fu-Li Sun(孙复莉), Yuan-Dong Wang(王援东), Jian-Hua Wei(魏建华), Yi-Jing Yan(严以京)

Citation: Chin. Phys. B . 2020, 29(6): 067204 . **doi:** 10.1088/1674-1056/ab8ac1
Journal homepage: http://cpb.iphy.ac.cn; http://iopscience.iop.org/cpb

What follows is a list of articles you may be interested in

Electrically tunable spin diode effect in a tunneling junction of quantum dot

Xukai Peng(彭许凯), Zhengzhong Zhang(张正中)

Chin. Phys. B . 2019, 28(12): 127202 . **doi:** 10.1088/1674-1056/ab53d0

Magnetotransport properties of graphene layers decorated with colloid quantum dots

Ri-Jia Zhu(朱日佳), Yu-Qing Huang(黄雨青), Jia-Yu Li(李佳玉), Ning Kang(康宁), Hong-Qi Xu(徐洪起)

Chin. Phys. B . 2019, 28(6): 067201 . **doi:** 10.1088/1674-1056/28/6/067201

Direct spin-phonon coupling of spin-flip relaxation in quantum dots

Ji-Wen Yin(尹辑文), Wei-Ping Li(李伟萍), Hong-Juan Li(李红娟), Yi-Fu Yu(于毅夫)

Chin. Phys. B . 2017, 26(1): 017201 . **doi:** 10.1088/1674-1056/26/1/017201

Decrease of back recombination rate in CdS quantum dots sensitized solar cells using reduced graphene oxide

Ali Badawi

Chin. Phys. B . 2015, 24(4): 047205 . **doi:** 10.1088/1674-1056/24/4/047205

Detection of Majorana fermions in an Aharonov-Bohm interferometer

Shang En-Ming, Pan Yi-Ming, Shao Lu-Bing, Wang Bai-Gen

Chin. Phys. B . 2014, 23(5): 057201 . **doi:** 10.1088/1674-1056/23/5/057201

Capacitive coupling induced Kondo–Fano interference in side-coupled double quantum dots*

Fu-Li Sun(孙复莉)[1], Yuan-Dong Wang(王援东)[1], Jian-Hua Wei(魏建华)[1,†], and Yi-Jing Yan(严以京)[2]

[1] *Department of Physics & Beijing Key Laboratory of Optoelectronic Functional Materials and Micro-nano Devices, Renmin University of China, Beijing* 100872, *China*

[2] *Hefei National Laboratory for Physical Sciences at the Microscale & Department of Chemical Physics, University of Science and Technology of China, Hefei* 230026, *China*

(Received 21 February 2020; revised manuscript received 17 April 2020; accepted manuscript online 18 April 2020)

We report capacitive coupling induced Kondo–Fano (K–F) interference in a double quantum dot (DQD) by systematically investigating its low-temperature properties on the basis of hierarchical equations of motion evaluations. We show that the interdot capacitive coupling U_{12} splits the singly-occupied (S-O) state in quantum dot 1 (QD1) into three quasi-particle substates: the unshifted S-O_0 substate, and elevated S-O_1 and S-O_2. As U_{12} increases, S-O_2 and S-O_1 successively cross through the Kondo resonance state at the Fermi level ($\omega = 0$), resulting in the so-called Kondo-I (KI), K–F, and Kondo-II (KII) regimes. While both the KI and KII regimes have the conventional Kondo resonance properties, remarkable Kondo–Fano interference features are shown in the K–F regime. In the view of scattering, we propose that the phase shift $\eta(\omega)$ is suitable for analysis of the Kondo–Fano interference. We present a general approach for calculating $\eta(\omega)$ and applying it to the DQD in the K–F regime where the two maxima of $\eta(\omega = 0)$ characterize the interferences between the Kondo resonance state and S-O_2 and S-O_1 substates, respectively.

Keywords: Kondo effect, Fano effect, quantum dot, capacitive coupling

PACS: 72.15.Qm, 73.63.Kv, 75.20.Hr **DOI:** 10.1088/1674-1056/ab8ac1

1. Introduction

Kondo resonance is a many-body process corresponding to a localized magnetic moment screened by itinerant electrons. It was originally proposed to explain the abnormal increase of resistance at low temperature in metals with dilute magnetic impurities.[1] Approximately 20 years ago, the Kondo effect was unveiled in a quantum dot (QD) system; this system was shown to provide a flexible and controllable physical implementation of the Kondo effect.[2] For a QD system in the Coulomb blockade regime, when the temperature T is below the characteristic temperature T_K, a sharp peak appears at the Fermi level ϵ_F in the spectral function of the system with an odd-number of localized electrons.[3]

Theoretically, a Kondo peak with particle–hole symmetry in the spectral function has the following three features: the height is $1/\pi\Gamma$ (Γ is the hybrid function) at zero temperature and decreases as the temperature increases, the width is proportional to T_K, and the lineshape can be fitted by a Lorentz profile.[3,4] However, in experimental conditions, the Kondo resonant peak may be affected by other channels and taken on an asymmetric lineshape. Li *et al.* reported an asymmetric Kondo resonant peak in a magnetic impurity embedded within the first atomic surface layer and attributed it to destructive Kondo–Fano (K–F) interference therein.[5] Subsequently, others have reported experimental Kondo resonance line-shapes that are asymmetric due to K–F interference.[6–8]

The K–F interference plays an important role in side-coupled double quantum dots (DQDs). For example, Sasaaki *et al.* observed a Fano resonance that arose from the interference between discrete levels in one dot and the Kondo effect in the other dot as a continuum.[8] They proved that the Kondo resonance is partially suppressed by destructive Fano interference, indicating the presence of a novel Fano–Kondo competition. Later theory work by Žitko *et al.* suggested that this phenomenon could be interpreted as a two-stage Kondo effect.[9]

Both the aforementioned experiment and theory on side-coupled DQDs have focused on the interdot tunneling coupling that directly mixes discrete and continuous levels. There could be other interactions that induce K–F interference in side-coupled DQDs. Such interactions would result in some interesting new spectral features. This issue is the main motivation of the present work.

In general DQDs, there are two basic kinds of interdot interactions. One is the tunneling type that can be described with the transfer coupling parameter, This type is related to the two-channel Kondo effects,[10,11] two-stage Kondo effects,[9,12–18] and others. The other interaction type is the capacitive type, and can be described by interdot Coulomb repulsion. This interaction is responsible for the single-electron switch and

*Project supported by the National Natural Science Foundation of China (Grant Nos. 11774418, 11374363, and 21373191).

†Corresponding author. E-mail: wjh@ruc.edu.cn

© 2020 Chinese Physical Society and IOP Publishing Ltd

other transport properties.[19–28] Hatano *et al.* recognized that capacitive Coulomb repulsion strongly affects charging diagrams[29] and Ruiz–Tijerina *et al.* treated it as an effective means of gating.[30] However, the possible K–F interference due to capacitive interactions has not been discussed previously.

In this work, the capacitive coupling induced K–F interference will be elucidated with a representative side-coupled DQD under quantum transport, as depicted in Fig. 1(a). The Hamiltonian for the isolated DQD is

$$H_{\rm sys} = \epsilon_d \sum_{us} \hat{n}_{us} + U \sum_{u} \hat{n}_{u\uparrow}\hat{n}_{u\downarrow} + U_{12}\hat{n}_1\hat{n}_2, \tag{1}$$

where $\hat{n}_{us} = \hat{d}^{\dagger}_{us}\hat{d}_{us}$ represents the electron occupation operator on dot $u = 1,2$, with spin $s = \uparrow,\downarrow$. We set $\epsilon_{us} = \epsilon_d$ for the on-dot energy. $\hat{d}^{\dagger}_{us}$ and $\hat{d}_{us}$ are the creation and annihilation operators for an electron in the dot-system state. U and U_{12} denote the intradot and interdot Coulomb interaction parameters, respectively.

To focus on the capacitive coupling interaction, we set the interdot tunneling coupling to be zero as shown in Fig. 1. We justify this approximation via a prior report showing that experimentally, the tunneling coupling can be weak enough to be neglected.[25] Further, a similar approximation has been adopted previously by other researchers.[31] In the absence of tunneling coupling, there is only one transport path (L–QD1–R) left for electrons; this path completely avoids the multiple-channel complication. We have also validated our results in the weak tunneling regime.

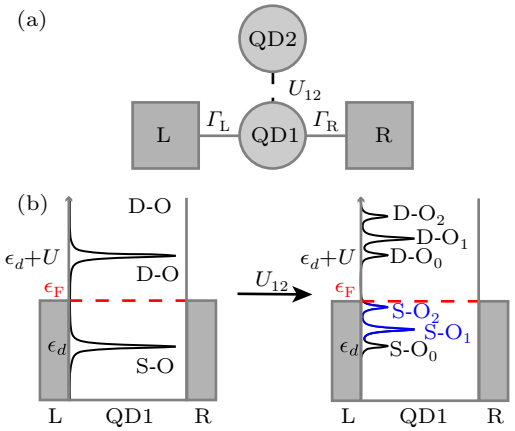


Fig. 1. (a) Schematic of the capacitively side-coupled DQD, where QD1 and QD2 couple with each other through the interdot Coulomb interaction U_{12}, but only QD1 couples directly to reservoirs L and R with hybridization $\Gamma_{\rm L}$ and $\Gamma_{\rm R}$, respectively. (b) Schematic view of the removal of degeneracy to the S-O (singly-occupied) and D-O (doubly-occupied) states by U_{12}. At very low temperature, the S-O$_2$ and S-O$_1$ substates go through $\epsilon_{\rm F}$ as U_{12} increases, and then interact with the Kondo resonance to induce Kondo–Fano interference.

Krychowski *et al.* studied the capacitive coupling effect without tunneling coupling using finite-U slave-boson mean-field theory (SBMFT).[32] SBMFT can qualitatively describe features of the Fermi-liquid ground state, but it does not simulate Hubbard peaks in spectral functions; thus, cannot yet describe K–F interference. As will be demonstrated, the shift of Hubbard peaks and their interplay with the Kondo peak play essential roles in K–F interference which is the main concern of the present work. Therefore, rather than SBMFT, we have adopted the hierarchical equations of motion (HEOM) approach, which is a powerful method for universal characterization of strongly correlated impurity systems. HEOM is especially useful for describing both Kondo and Hubbard peaks.[4,33]

The phase shift $\eta(\omega)$ is essential to describing the K–F interference. According to standard scattering theory, $\eta(\omega)$ directly relates to the scattering core (T matrix) $T(\omega)$ by[3]

$$\eta(\omega) = \text{Arg det}[T(\omega)]. \tag{2}$$

In theory, the phase shift can be obtained by different methods and parameter limits.[34] In the local moment regime with half-occupation of each spin, $\eta(\omega) = \pi/2$ as a Fermi-liquid feature of Kondo scattering.[3]

In a single QD system, the change in the phase shift due to the K–F interference was first noticed by Luo *et al.* when they investigated the interference between Kondo resonance and the broadened QD level in the mixed valence regime.[35] To avoid the difficult calculation, Luo *et al.* suggested a simple form of $T(\omega)$ from Kondo scattering; they found that this phase shift is necessary to accurately reproduce the results of scanning tunneling microscopic experiments.[36] Since then, the phase shift has been widely used in literature, but only as a fitting parameter. In the present paper, we present a general approach to calculate $\eta(\omega)$ accurately, and then apply it to thoroughly investigate K–F interference in a DQD, where charge and spin degrees of freedom strongly interact with each other.

In the next section, we introduce the model Hamiltonian and the relevant parameters. Following, we demonstrate the three regimes (Kondo-I, Kondo–Fano, and Kondo-II regimes), characterized by different features of spectral $A(\omega)$, phase shift of K–F interference $\eta(\omega)$, and asymmetry function $q_{\rm d}(\omega)$. We discuss these regimes separately in three subsections. Moreover, we compare the results obtained from differential conductance measurements. Finally, we conclude this work. We briefly describe our HEOM approach in Appendix A, emphasize the calculation of Green's function in Appendix B, and present an understanding of the 'background' in Appendix C.

2. Model and Hamiltonian

The total system-plus-reservoir composite Hamiltonian reads $H_{\rm total} = H_{\rm sys} + H_{\rm res} + H_{\rm sys\text{-}res}$. For the model DQD of

Fig. 1 in this study, the other two parts can be written as

$$H_{\rm res} = \sum_{\alpha={\rm L,R}} \sum_{ks} \epsilon_{\alpha ks} \hat{c}^{\dagger}_{\alpha ks} \hat{c}_{\alpha ks}, \tag{3}$$

$$H_{\rm sys\text{-}res} = \sum_{\alpha={\rm L,R}} \sum_{ks} \Gamma_{\alpha} (\hat{d}^{\dagger}_{1s} \hat{c}_{\alpha ks} + \hat{c}^{\dagger}_{\alpha ks} \hat{d}_{1s}), \tag{4}$$

where $\hat{c}^{\dagger}_{\alpha ks}$ and $\hat{c}_{\alpha ks}$ are the creation and annihilation operators in the specified reservoir state, with energy $\epsilon_{\alpha ks}$. The dot system linearly couples with a reservoir by Γ_{α}, with transport path of L–QD1–R. In the HEOM method, we calculate $D_{\alpha uvs}(\omega)$ by the definition $D_{\alpha uvs}(\omega) \equiv \frac{1}{2\pi} \int_{-\infty}^{\infty} {\rm d}\tau {\rm e}^{{\rm i}\omega\tau} \langle \{ \hat{f}_{\alpha us}(\tau), \hat{f}^{\dagger}_{\alpha vs}(0) \} \rangle_{\rm res}$, where $\hat{f}_{\alpha us}$ and $\hat{f}^{\dagger}_{\alpha vs}$ are the reservoir operators defined by $\hat{f}_{\alpha us}(\tau) \equiv {\rm e}^{{\rm i}H_{\alpha}\tau} (\sum_{k\in\alpha} t_{\alpha ku} \hat{c}_{\alpha ks}) {\rm e}^{-{\rm i}H_{\alpha}\tau}$ and $\hat{f}^{\dagger}_{\alpha us}(\tau) \equiv {\rm e}^{{\rm i}H_{\alpha}\tau} (\sum_{k\in\alpha} t^{*}_{\alpha ku} \hat{c}^{\dagger}_{\alpha ks}) {\rm e}^{-{\rm i}H_{\alpha}\tau}$. In practice, we choose the initial input of the reservoir spectral density function as $D_{\alpha uvs}(\omega) = \delta_{uv} \Gamma_{\alpha} W_{\alpha}^2 / [(\omega - \mu_{\alpha})^2 + W_{\alpha}^2]$, with effective dot–reservoir coupling of Γ_{α} (see Fig. 1), a width of the conduction band of W_{α} in the α-reservoir, and the chemical potential μ_{α}. Of note, Γ_{α} is the aforementioned hybridization, $\Gamma_{\alpha} = \pi (t_{\alpha})^2 \rho_{\alpha}$, where ρ_{α} is the density of states of the reservoir α at its Fermi level (or chemical potential). Here, we set the equilibrium Fermi energy to be $\epsilon_{\rm F} = \mu_{\alpha}^{\rm eq} = 0$. In the presence of bias voltage, $\mu_{\rm L} - \mu_{\rm R} = V$.

According to Dyson's equation in the textbook scattering theory

$$G^{+}(\omega) = G_0^{+}(\omega) + G_0^{+}(\omega) T(\omega) G_0^{+}(\omega), \tag{5}$$

where the retarded Green's function $G^{+}(\omega)$, the background part $G_0^{+}(\omega)$, and the scattering core $T(\omega)$ are all complex functions. It is apparent that $T(\omega)$ contains all the information of the scattering process from the initial state G_0^{+} to the final state G^{+}. $T(\omega)$ directly relates to the phase shift through Eq. (2).

By using the HEOM approach, we can obtain any retarded Green's function of the DQDs numerically (cf. Appendix B). We use $G(\omega)$ to represent the retarded Green's function of QD1, while ignoring the spin index due to the spin-degeneracy. Then, $T(\omega)$ can be calculated accurately from Eq. (5)

$$T(\omega) = G_0^{-1}(\omega) G(\omega) G_0^{-1}(\omega) - G_0^{-1}(\omega), \tag{6}$$

and accordingly, the phase shift $\eta(\omega)$ can be obtained from Eq. (2).

Another important physics quantity that we describe in this report is Fano's asymmetric function. The existence of interdot Coulomb interaction U_{12} will affect the single QD Kondo scattering and lead to the K–F effect. As proved in Ref. [35], there is a convenient way to illustrate the resultant asymmetric line shape only using the scattering background

$$q_{\rm d}(\omega) \equiv -\frac{{\rm Re}G_0^{+}(\omega)}{{\rm Im}G_0^{+}(\omega)}, \tag{7}$$

where $q_{\rm d}(\omega)$ is the asymmetric function of interest. Note that $q_{\rm d}(\omega)$ is different from the conventional Fano parameter q. Since q cannot be obtained from our HEOM approach, we choose $q_{\rm d}(\omega)$ by following the literature definition. We will discuss this point later.

In this work, we are interested in a DQD [see Fig. 1(a)] with particle–hole symmetry ($\epsilon_d = -U/2$) and the fixed parameters $\Gamma_{\rm L} = \Gamma_{\rm R} = 0.5\Gamma$, in units of $\Gamma = 0.4$ meV, $U = 2.0$ meV and $W_{\rm L} = W_{\rm R} = 10\Gamma$ (W is the bandwidth of the reservoirs). We compare the results at low temperature ($T = 0.02$ meV $\ll T_{\rm K}$) and high temperature ($T = 0.3$ meV $\gg T_{\rm K}$), where the reference $T_{\rm K} \approx 0.12$ meV from $U_{12} = 0$ scenario by an analysis expression $T_{\rm K} = \sqrt{\frac{U\Gamma}{2}}\, {\rm e}^{-\pi U/8\Gamma + \pi\Gamma/2U}$ in Ref. [3].

3. Three regimes

3.1. Overall features

Now we examine the effect of capacitive interdot coupling, U_{12}, on the spectral function of QD1, $A(\omega)$, evaluated via the HEOM implementation of linear response theory.[4,37]

As a reference, we have derived the Green's function of the isolated DQD [cf. Eq. (C1)] and plotted the positions of its poles in Fig. 2(a) with yellow lines. We observe that U_{12} splits the individual S-O and D-O states into three quasi-particles substates $\{{\rm S\text{-}O}_0, {\rm S\text{-}O}_1, {\rm S\text{-}O}_2\}$ and $\{{\rm D\text{-}O}_0, {\rm D\text{-}O}_1, {\rm D\text{-}O}_2\}$, respectively. The resultant Hubbard peaks, S-O$_m$ and D-O$_m$, are centered at about $\omega = \epsilon_d + mU_{12}$ and $\omega = \epsilon_d + U + mU_{12}$.

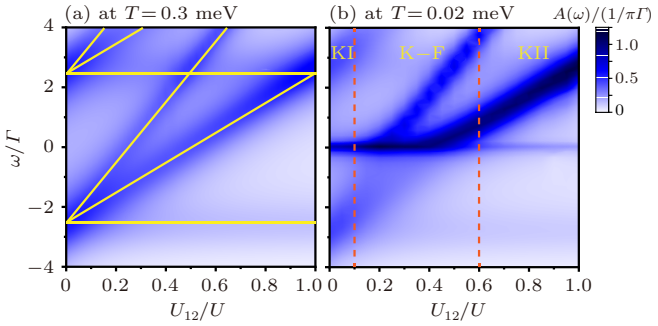


Fig. 2. (a) Color-scale plot of local spectral density of QD1, $A(\omega)$, varying with the capacitive interdot coupling U_{12}, at the strong-hybridization ($\Gamma = 0.4$ meV) high-temperature ($T = 0.3$ meV $\gg T_{\rm K}$) regime. (b) Color-scale plot of $A(\omega)$ varying with U_{12} at the strong-hybridization, low-temperature ($T = 0.02$ meV $\ll T_{\rm K}$) regime..

Figure 2(a) depicts the variance of the local spectral density of QD1 in color-scale, $A(\omega)$, with the capacitive interdot coupling, U_{12}, at the strong-hybridization ($\Gamma = 0.4$ meV), high-temperature ($T = 0.3$ meV $\gg T_{\rm K}$) regime. Generally, the numerical result matches well with the analytical one. The peaks in the color-scale plot of Fig. 2(a) correspond to the poles in Eq. (C1).

Figure 2(b) shows the $A(\omega)$ at low-temperature, $T = 0.02$ meV $\ll T_K$, with the same hybridization $\Gamma = 0.4$ meV as that shown in Fig. 2(a). In this regime, the strong correlation quantum effect dominates. Moreover, QD1 contains a localized magnetic moment, with strong coupling to the electron reservoirs at $T \ll T_K$. The Kondo singlet state emerges at the Fermi level ϵ_F, resulting in a resonant peak at $\omega = 0$. Meanwhile, the capacitive interdot coupling U_{12} removes the degeneracy in the individual S-O and D-O states of the isolated QD1. The aforementioned elevated S-O_2 and S-O_1 substates go through the Fermi level successively, as U_{12} increases. In particular, when the S-O_2 or S-O_1 substates appear near ϵ_F, the Kondo resonant peak in $A(\omega)$ becomes asymmetric, due to the underlying Fano interference.

Therefore, the capacitively side-coupled DQD at $T \ll T_K$ experiences three distinct Kondo regimes, corresponding to the relative value of U_{12} with respect to the intradot Coulomb coupling strength U. For the particle–hole symmetry ($\epsilon_d = -U/2$) in the DQD examined here, these three regimes are divided by the vertical-dashed lines in Fig. 2(b): the Kondo-I (KI) regime ($U_{12} < 0.1U$), where the interdot Coulomb coupling has little effect, the Kondo–Fano (K–F) regime ($0.1U \leq U_{12} \leq 0.6U$), where the S-$O_2$ and S-O_1 substates significantly interfere with the Kondo state; and the Kondo-II (KII) regime ($U_{12} > 0.6U$), where the S-O_2 and S-O_1 substates are elevated above the Fermi level and the S-O_0 substate supports Kondo resonance.

The only difference between Figs. 2(a) and 2(b) occurs when the temperature is far above or below T_K, indicating there is a hallmark around the Fermi level without or with the Kondo effect. Since the scattering matrix carries the information about the Kondo effect [cf. the K–F regime] we are able to regard Fig. 2(a) as the background of Fig. 2(b).

3.2. The Kondo-I regime

In the KI regime, $A(\omega)$ has a three-peak structure, as demonstrated in Fig. 3(a). The middle peak is a Kondo resonant peak having a symmetric line shape with width $\sim 1.75\Gamma$ [cf. Fig. 2(b)] that disappears at high-T [cf. Fig. 2(a)]. U_{12} in the KI regime is so small that it is difficult to resolve the S-O or D-O substates. The three-peak structure contains an S-O state below ϵ_F, a D-O state located symmetrically above ϵ_F, and a Kondo resonant state at ϵ_F. Figure 3(b) emphasizes the Kondo peaks at $U_{12} = 0$ and $0.05U$. There is little difference between these two peaks in either height or width. We propose that $A(\omega)$ keeps its three-peak structure, much like a single QD, when U_{12} is small.

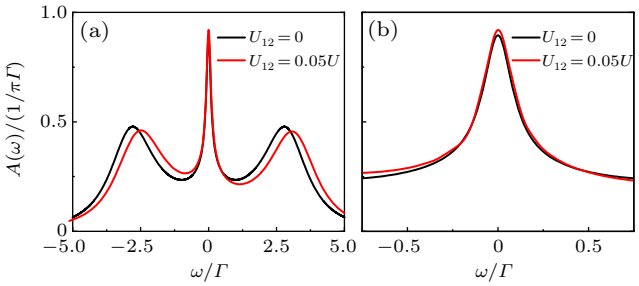


Fig. 3. (a) The three-peak structure consists of, from left to right, the S-O state, the Kondo resonant state, and the D-O state. Here $\epsilon_d = -2.5\Gamma$ and $\epsilon_d + U = 2.5\Gamma$. (b) Details of the Kondo resonant state around the Fermi level.

3.3. The Kondo–Fano regime

Further increasing U_{12} drives the symmetric Kondo peak in $A(\omega)$ to gradually change into an asymmetric Kondo–Fano peak, indicating that the DQD has entered the K–F regime. Figures 4(a)–4(c) plot $A(\omega)$ in the vicinity of ϵ_F in the K–F regime. When U_{12} grows larger than $U_{12} = 0$, the highest point of $A(\omega)$ moves away from $\omega = 0$ in the same direction as S-O_m, $\{m = 1, 2\}$. This phenomenon (the S-O state driving the highest point of $A(\omega)$ higher) is clear in a single QD,[2] but has not been investigated in the S-O substates of a DQD.

In Fig. 4(d), $A(\omega = 0)$ increases (constructive interference), decreases (competition), and then falls below its original height (destructive interference). This is due to interference, not simple superposition, as evidenced by distinct asymmetry.

Figure 4(a) shows in detail the constructive interference of the Kondo resonant peak caused by interference from the S-O_2 substate. $A(\omega = 0)$ reaches its maximum when the S-O_2 state arrives at ϵ_F. It has been demonstrated that this K–F constructive interference is not due to other effects, such as the t-enhanced Kondo effect.[38] Figure 4(b) demonstrates a feature due to competition between constructive and destructive interferences of the Kondo resonant peak. This competition occurs because while the S-O_1 state is about appearing, the S-O_2 state still has an effect around the Fermi level. At $U_{12} = 0.4$, the S-O_1 state arrives at ϵ_F and becomes dominant. Figure 4(c) shows the destructive interference of the Kondo resonant peak caused by interference from the S-O_1 state. A kink appears at $\omega = 0$, taking the place of the peak localized near ϵ_F; we propose that this kink is a signal line shape of the destructive K–F effect. This destructive feature of the line shape at the zero point of the asymmetry factor has previously been reported in different Fano resonance systems in the literature.[39,40] As the S-O_1 state moves away from ϵ_F, the destructive interference becomes weak and the profile around ϵ_F smoothly changes to a small bump that is symmetric, and the system enters the next regime.

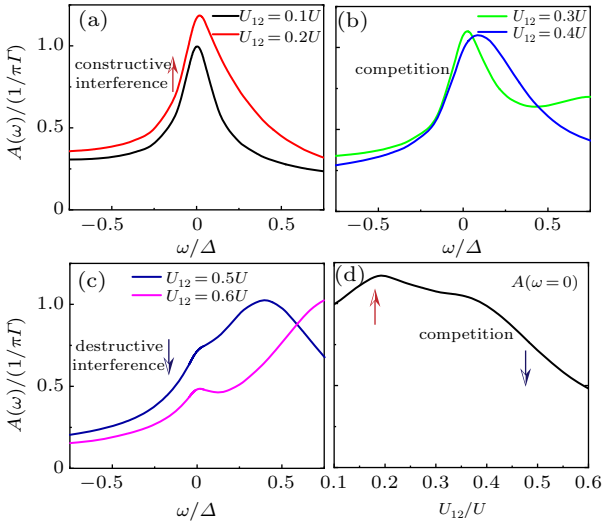


Fig. 4. The $A(\omega)$ in the vicinity of ϵ_F in the Kondo–Fano regime. The Kondo peak at the Fermi level has (a) constructive interference from the S-O_2 substate, (b) competition between constructive and destructive interferences, and (c) destructive interference from the S-O_1 substate. (d) $A(\omega=0)$ variation by U_{12}.

We are now in the position to demonstrate our numerically phase shift $\eta(\omega)$ in the K–F regime, where charge and spin degrees of freedom strongly interact with each other. The U_{12}-dependent $\eta(\omega=0)$ and the asymmetry function $q_d(\omega=0)$ are shown in Figs. 5(a) and 5(b), respectively. As expected, the change in the phase shift $\pi/2-\eta(\omega=0)$ contains the essential physics of the K–F interference over a wide range of U_{12}. Here we see the same trend with U_{12} as the asymmetry function.

At $U_{12}=0$, the numerical phase shift $\eta(0)$ is exactly equal to $\pi/2$, as shown in Fig. 5(a), This feature is well-known as the phase shift of pure Kondo scattering.[3] When the system enters into the K–F regime, $\eta(0)$ experiences two maxima corresponding to interference between the Kondo resonance state and each of the S-O_2 and S-O_1 substates, respectively. The constructive process due to the shift of the S-O_2 substate dominates at the first maximum. Destructive interference from S-O_1 then takes the dominant position to induce the second maximum before the competition region that results in a small valley of $\eta(0)$. Unfortunately, the signature of $\eta(0)$ itself cannot distinguish whether the interference is constructive or destructive, thus spectral analysis (cf. Fig. 4) is always necessary to clarify the microscopic picture.

In our DQD, the Kondo resonance should be a discrete channel with a narrow peak profile in $A(\omega)$ at ϵ_F; and the background provides the open channel. Since the former is a robust many-body state localized around $\omega=0$, the change in interference is determined mainly by the latter. This has been verified by the asymmetric function $q_d(0)$ shown in Fig. 5(b), which changes nearly synchronously with $\eta(0)$. At $U_{12}=0$, $q_d(0)=0$, indicating a symmetry resonance of the Kondo effect without any interference. With the increase of U_{12}, $q_d(0)$ decreases after two local maxima in a similar fashion as $\eta(0)$. At $U_{12}>0.6U$, $q_d(0)$ approaches a constant value of -2, indicating the presence of another symmetric Kondo resonance without interference. This Kondo effect is a special characteristic of DQDs, that goes beyond the simple form of Kondo scattering in single QDs, as described in Ref. [35].

In our calculations, $q_d(0)=0$ corresponds to the symmetric line shape around the Fermi level, and shows a different feature from that of the Fano asymmetric factor q. We note that the difference results from the definition of q_d in Eq. (7). By fitting our numerical results to $A(\omega)$, we obtain $q=263.72\to\infty$ at $U_{12}=0$, consistent with the Fano interference theory, which postulates that large q values lead to peaks in spectral line-shapes.

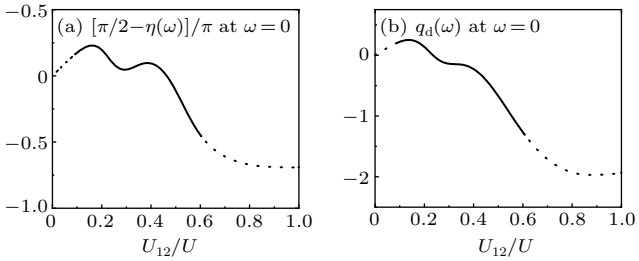


Fig. 5. (a) The phase shift $\eta(\omega=0)$ and (b) asymmetry function $q_d(\omega=0)$ as functions of U_{12}. The changes in $\eta(0)$ and $q_d(0)$ in the K–F regime are shown in solid lines, while those in the KI and KII regimes are shown in dotted lines.

3.4. The Kondo-II regime

As the S-O_m $\{m=1,2\}$ states move further away from ϵ_F at $U_{12}>0.6U$, the zero-point peak of $A(\omega)$ tends to not change in intensity. On a small scale around the Fermi level, the three-peak structure partially recovers.

In this side-coupled DQD, we assume that no electron could transport to or from QD2, and we set $\epsilon_d=-1/2U$, where the correlation effect is the most significant.[41] Consequentially, for the quasi-particles, the weight of the S-O_0 (D-O_0) substate is a quarter of that of the total S-O (D-O) state. Similarly to the S-O (D-O) state, the S-O_0 (D-O_0) substate broadens from the environment, it is obvious that they have the same width. At large U_{12}, without the S-O_1 and S-O_2 states, the position of the S-O_0 substate is fixed, and an effective localized magnetic moment is maintained in QD1.

In the KII regime, at low temperature, and with invariant QD1 coupling to the reservoirs, the necessary conditions exist for Kondo resonance. A quarter-localized 1/2 spin in QD1 leads to a Kondo peak at ϵ_F in $A(\omega)$. By carefully comparing the Kondo peak at $U_{12}=0$ and $2U$ (cf. insert of Fig. 6), we find that the peak height in the KII regime is $1/4$ of that in the KI regime. However, these peaks have the same semi-width, meaning they have the same characteristic temperature T_K. Our results indicate that there is essentially no difference between the Kondo-I and II regimes other than the height.

The Fermi-liquid behavior of the KII regime seems to conflict with our intuition that small local momentum should be over-screened by conduction electrons.

We explain this as follows. Let us first consider the KI regime, where Fermi-liquid behavior is characterized by the symmetric Kondo resonance peak localized at ϵ_F, as shown in Fig. 3(a). By considering the triple-splitting of the S-O state (see Figs. 1 and 2), we can understand that the single Kondo peak actually involves the screening of momentum in all three S-O substates. The spin of each is still equal to 1/2, otherwise an over-screening effect would change the essential features of the Kondo peak. It is obvious from Fig. 3 that this does not occur. Therefore, the charge of the electron, not the spin, has been divided by the triple-splitting. We also find that the occupation number in QD1 is going to reduce to 1/4, which proves further that the amount of charge, not the 1/2 spin, is reduced.

In summary, in the KII regime, near ϵ_F, $A(\omega)$ partially recovers the three-peak structure, where each peak has the same width and a quarter of the height of the corresponding peak in the KI regime.

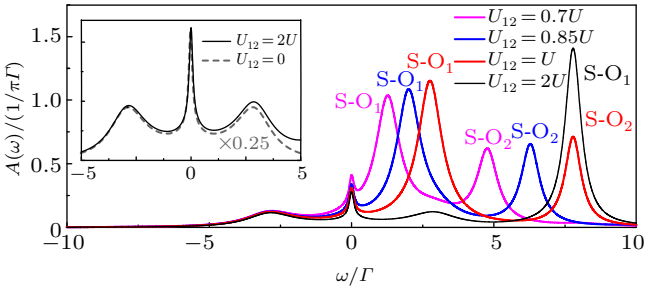


Fig. 6. The $A(\omega)$ in the vicinity of ϵ_F in the KII regime. The insert illustrates $A(\omega)$ at $U_{12}=2U$ (solid black line) as well as at $U_{12}=0$ (dash gray line) on a detailed scale around the Fermi level. The three-peak structure is partially recovered, and $A(\omega)$ at $U_{12}=2U$ has a quarter of the height of $A(\omega)$ at $U_{12}=0$.

4. Differential conductance

The spectral function $A(\omega)$ is capable of revealing detailed dynamical properties over a wide range of parameters. However, in QD experiments, $A(\omega)$ cannot be observed conveniently. Conductance is more favourable for experimental measurement; therefore, we calculate the differential conductance $\mathrm{d}I/\mathrm{d}V$ under nonequilibrium conditions taking advantage of the HEOM evaluation.

We set the initial total system at equilibrium at $\mu_\alpha = \mu^{\mathrm{eq}} = 0$ ($\alpha = \mathrm{L}$ and R). Application of a voltage to the left and right reservoirs, resulting in current flow into the α-reservoir $I_\alpha(t)$, causes the system to leave equilibrium [details in Eq. (A21)]. Through the extended Meier–Tannor parametrization method and multiple-frequency-dispersed hierarchy construction, we can achieve the closed HEOM formalism.[33]

As a result, the current from L to R can be denoted as $I(t) = I_{\mathrm{L}}(t) = -I_{\mathrm{R}}(t)$. The differential conductance $\mathrm{d}I/\mathrm{d}V$ can then be obtained from the steady current $I = I(t \to \infty)$ as a function of bias V.

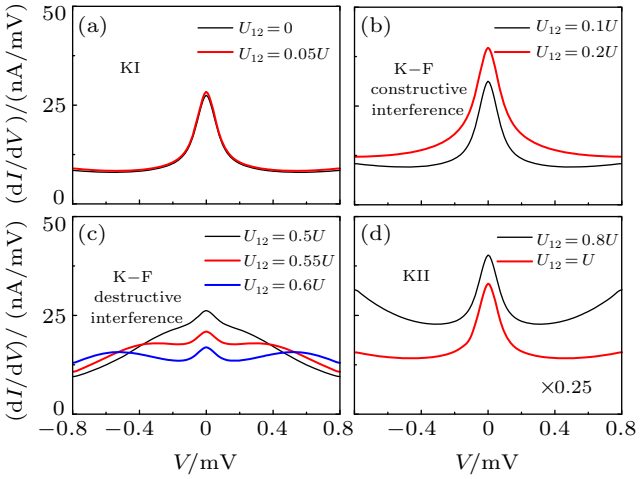


Fig. 7. (a) The Kondo-I regime, (b) the Kondo–Fano regime with constructive resonance, (c) the Kondo–Fano regime with destructive resonance, and (d) the Kondo-II regime.

Figure 7 depicts the numerical $\mathrm{d}I/\mathrm{d}V$ with Fig. 7(a) in the KI regime, Figs. 7(b) and 7(c) in the K–F regime, and Fig. 7(d) in the KII regime. In Fig. 7(a), the $\mathrm{d}I/\mathrm{d}V$ curves present a zero-bias peak structure, which is a typical feature of the ordinary Kondo effect.

In Figs. 7(b) and 7(c), one can see two kinds of peak structures in the K–F regime resulting from constructive and destructive Fano interferences. The constructive interference enhances the Kondo effect to a certain degree and consequently reinforces the zero-bias peak of $\mathrm{d}I/\mathrm{d}V$. On the other hand, the observed destructive interference suppresses the zero-bias peak gradually. As shown in Fig. 7(c), symmetric peak shoulders appear on each side of the distinctly suppressed main peak at $U_{12} = 0.5U$. At this value, the Kondo peak of $A(\omega)$ has changed to the kink at ϵ_F [see Fig. 4(c)]. As U_{12} increases to a value of $U_{12} = 0.6U$, the shoulders grow in intensity and move outwards, while the zero-bias peak becomes clearer and less suppressed.

The Fano interference disappears gradually, until finally the shoulders cannot be observed at $-0.8\ \mathrm{mV} < V < 0.8\ \mathrm{mV}$; the single peak structure is restored at $V = 0$. At this point, the system comes into the KII regime, as shown in Fig. 7(d). The height of the zero-bias peak in the KII regime is about a quarter of that in the KI regime; this is the same ratio as that seen in the spectral function $A(\omega)$.

As demonstrated in Fig. 7, the destructive K–F effects can be experimentally investigated by virtue of the peak–shoulder structure of the differential conductance. For constructive interference, we find that the peak becomes slightly broader and higher, but this change is subtle and is difficult to resolve.

5. Summary

We have reported a capacitive coupling induced Kondo–Fano interference in a side-coupled DQD by systematically investigating its low-temperature properties on the basis of HEOM evaluations. We found that as the interdot Coulomb coupling U_{12} increases, the system excitations evolve from the Kondo-I regime to the K–F regime, and from the K–F regime to the Kondo-II regime (cf. Fig. 2). Generally, U_{12} splits the singly-occupied (S-O) state and the doubly-occupied (D-O) state into three substates, with the S-O$_m$ and D-O$_m$, $(m = 1,2)$ substates elevated linearly and the S-O$_0$ and D-O$_0$ substates unchanged. At temperatures lower than the characteristic Kondo temperature, in the KI regime, the Kondo screening of the 1/2-spin localized in the whole S-O state induces a single Fermi-liquid peak at the Fermi level ($\epsilon_{\rm F}$). In the K–F regime, the S-O$_2$ and S-O$_1$ substates shift near $\epsilon_{\rm F}$, interfering with the Kondo resonance and appearing as the K–F effect, which first enhances the Kondo peak by constructive interference (from S-O$_2$) and then depresses it by destructive interference (from S-O$_1$). In the KII regime, after U_{12} elevates the S-O$_m$ $(m = 1,2)$ substates away from $\epsilon_{\rm F}$, the three-peak structure partially recovers on a small scale and the Kondo screening of the residual spin in the S-O$_0$ restores the Fermi-liquid peak at $\epsilon_{\rm F}$, with the same width but 1/4 the height of the peak seen in the KI regime.

We have also presented a general approach to calculate the phase shift $\eta(\omega)$ of the K–F interference numerically. We then applied this approach to our DQD in the K–F regime, where charge and spin degrees of freedom strongly interact with each other. We have shown that the change of the phase shift contains the essential physics of the K–F interference over a wide range of U_{12}. When the system enters into the K–F regime, $\eta(\omega = 0)$ experiences two maxima corresponding to the interference between the Kondo resonance state and the S-O$_2$ and S-O$_1$ substates, respectively.

In order to facilitate experimental observation, we have also calculated the differential conductance $\mathrm{d}I/\mathrm{d}V$ under nonequilibrium conditions. We found that both the KI and KII regimes are characterized by the single zero-bias peak of $\mathrm{d}I/\mathrm{d}V$, analogously to the ordinary Kondo systems. We have shown that the peak–shoulder structure of $\mathrm{d}I/\mathrm{d}V$ at small bias can serve as an observable feature of the Kondo–Fano effect with destructive interference in the K–F regime.

In reality, the capacitive interdot coupling may be accompanied by interdot charge transfer. It is expected that the additional transport path of L–QD2–R will inevitably affect the Kondo–Fano features at low temperature This will be addressed in our future work.

Appendix A: HEOM method

The HEOM formalism is established based on Feynman–Vernon influence functional path-integral theory,[42–45] and implemented with Grassmann algebra for fermionic dissipations.[33,43] Thus, HEOM is formally exact for a general open system coupled to a reservoir bath that satisfies Grassmann Gaussian statistics. Further, the HEOM method leads to an efficient and universal approach for characterization of quantum impurity systems at finite temperatures.[4] The mathematical construction of HEOM has been discussed comprehensively in Refs. [33,44–46]. We address some key features of the HEOM here, particularly those pertinent to the QD systems studied in the main text of this work.

HEOM investigates the properties of QDs in both equilibrium and nonequilibrium states via the reduced density operator. At time t, the reduced system density operator, $\rho(t) = \mathrm{tr}_{\rm res}\rho_{\rm total}(\mathrm{t})$, is related to the initial value at time t_0 via the reduced Liouville-space propagator $\mathcal{G}(t,t_0)$ by

$$\rho(t) = \mathcal{G}(t,t_0)\rho(t_0). \tag{A1}$$

Let $\{|\psi\rangle\}$ be an arbitrary basis set defined in the system space, and $\psi = (\psi,\psi')$. Therefore $\rho(\psi,t) = \rho(\psi,\psi',t)$. From the Feynman–Vernon influence functional, the path-integral expression for the reduced Liouville-space propagator is

$$\mathcal{U}(\psi,t;\psi_0,t_0) = \int_{\psi_0[t_0]}^{\psi[t]} \mathcal{D}\psi\, \mathrm{e}^{\mathrm{i}S[\psi]}\mathcal{F}[\psi]\,\mathrm{e}^{-\mathrm{i}S[\psi']}. \tag{A2}$$

Here, $S[\psi]$ is the classical action of the reduced system. $\mathcal{F}[\psi]$ is the influence functional determined by the Grassmann variables of the system-environment coupling $\hat{f}^{\dagger}_{\alpha us}(t)d_{is}[\psi_s] +$ H.c. The operators $\hat{f}^{\dagger}_{\alpha us}(t)$ and $\hat{f}_{\alpha us}(t)$ are the reservoir operators defined by

$$\hat{f}^{\dagger}_{\alpha us}(t) \equiv \mathrm{e}^{\mathrm{i}H_{\alpha}t}\left(\sum_{k\in\alpha} V^{*}_{\alpha k us}\hat{c}^{\dagger}_{\alpha ks}\right)\mathrm{e}^{-\mathrm{i}H_{\alpha}t}, \tag{A3}$$

$$\hat{f}_{\alpha us}(t) \equiv \mathrm{e}^{\mathrm{i}H_{\alpha}t}\left(\sum_{k\in\alpha} V_{\alpha k us}\hat{c}_{\alpha ks}\right)\mathrm{e}^{-\mathrm{i}H_{\alpha}t}. \tag{A4}$$

The influence functional can be evaluated using the Wick theorem and the second-order cumulant expansion method, because all the other higher order cumulants are zero at the thermodynamic Gaussian average for non-interaction leads. As a result, the ensemble averages of the second-order cumulants are connected to the reservoir correlation functions (lead correlation functions, LCFs) $C^{\pm}_{\alpha uvs}(t)$, defined as

$$C^{+}_{\alpha uvs}(t) = \left\langle \hat{f}^{\dagger}_{\alpha us}(t)\hat{f}_{\alpha vs}(0)\right\rangle_{\rm res}, \tag{A5}$$

$$C^{-}_{\alpha uvs}(t) = \left\langle \hat{f}_{\alpha us}(t)\hat{f}^{\dagger}_{\alpha vs}(0)\right\rangle_{\rm res}, \tag{A6}$$

where $\langle\ldots\rangle_{\rm res}$ stands for the ensemble average of the reservoirs, and the time translation invariance is used. All LCFs in a form different from that in Eqs. (A5) and (A6) are zero because the lead operators $\hat{f}^{\dagger}_{\alpha us}(t)$ and $\hat{f}_{\alpha us}(t)$ satisfy Gaussian

statistics. The reservoir spectral density function is defined as

$$D_{\alpha uvs}(\omega) \equiv \frac{1}{2\pi}\int_{-\infty}^{\infty} \mathrm{d}t\, \mathrm{e}^{\mathrm{i}\omega t}\langle\{\hat{f}_{\alpha us}(t), \hat{f}^{\dagger}_{\alpha vs}(0)\}\rangle. \tag{A7}$$

With the simplified notation $\sigma = +, -$ and $\bar{\sigma} = -\sigma$, the reservoir correlation functions are associated with the spectral density functions via the fluctuation–dissipation theorem

$$C^{\sigma}_{\alpha uvs}(t) = \int_{-\infty}^{\infty} \mathrm{d}\omega\, \mathrm{e}^{\mathrm{i}\sigma\omega t} f^{\sigma}_{\alpha}(\omega) D^{\sigma}_{\alpha uvs}(\omega), \tag{A8}$$

where $D^{-}_{\alpha uvs}(\omega) = D_{\alpha uvs}(\omega)$, $D^{+}_{\alpha uvs}(\omega) = D_{\alpha uvs}(\omega)$, and $f^{\sigma}_{\alpha}(\omega) = 1/(1+\mathrm{e}^{\sigma\beta_{\alpha}(\omega-\mu_{\alpha})})$ is the Fermi–Dirac function for the electron ($\sigma = +$) or hole ($\sigma = -$) at the temperature $\beta_{\alpha} = 1/k_{\mathrm{B}}T_{\alpha}$. For linear coupling with a non-interacting reservoir, the reservoir spectral density function can be evaluated as $D_{\alpha uvs}(\omega) = \sum_k t^{*}_{\alpha k us} t_{\alpha k vs}\delta(\omega - \epsilon_{\alpha k})$. After applying the Wick theorem and Grassmann algebra, the final expression of the influence functional $\mathcal{F}$ is

$$\mathcal{F}[\psi] = \exp\left\{-\int_{t_0}^{t} \mathrm{d}\tau \mathcal{R}[\tau, \{\psi\}]\right\}, \tag{A9}$$

where $\mathcal{R}[\tau,\{\psi\}] = \frac{\mathrm{i}}{\hbar^2}\sum_{\alpha us\sigma}\mathcal{A}^{\bar{\sigma}}_{us}[\psi(t)]\mathcal{B}^{\sigma}_{\alpha us}[t,\psi]$. Here, $\mathcal{A}^{\bar{\sigma}}_{us}$ and $\mathcal{B}^{\sigma}_{\alpha us}$ are the Grassmann variables defined as

$$\mathcal{A}^{\bar{\sigma}}_{us}[\psi(t)] = d^{\sigma}_{us}[\psi(t)] + d^{\sigma}_{us}[\psi'(t)], \tag{A10}$$

$$\mathcal{B}^{\sigma}_{\alpha us}[t,\psi] = -\mathrm{i}\left[B^{\sigma}_{\alpha us}(t,\psi) - B'^{\sigma}_{\alpha us}(t,\psi')\right], \tag{A11}$$

with

$$B^{\sigma}_{\alpha us}(t,\psi) = \sum_{v}\int_{0}^{t} \mathrm{d}\tau C^{\sigma}_{\alpha uvs}(t-\tau) d^{\sigma}_{vs}[\psi(\tau)], \tag{A12a}$$

$$B'^{\sigma}_{\alpha us}(t,\psi') = \sum_{v}\int_{0}^{t} \hat{\mathrm{d}}\tau C^{\bar{\sigma}*}_{\alpha uvs}(t-\tau)\hat{d}^{\sigma}_{vs}[\psi'(\tau)]. \tag{A12b}$$

The LCFs play the role of memory kernels that can be expanded by a series of exponential functions with the implementation of the fluctuation–dissipation theorem together with the Cauchy residue theorem and the Padé spectrum decomposition scheme of the Fermi function

$$C^{\sigma}_{\alpha uvs}(t) = \sum_{m=1}^{M} \eta^{\sigma}_{\alpha uvsm} e^{-\gamma^{\sigma}_{\alpha uvsm} t}. \tag{A13}$$

The bath influence then enters the equations of motion with M exponentiations.

Set $j = \{\alpha us\sigma\}$ or $j = \{us\sigma\}$ for simplicity. Through introducing auxiliary influence functionals,

$$\tilde{\mathcal{F}}^{(n)}_{\boldsymbol{j}} \equiv \Big(\tilde{\mathcal{B}}_{j_n}\cdots\mathcal{B}_{j_2}\mathcal{B}_{j_1} + \cdots + \mathcal{B}_{j_n}\cdots\tilde{\mathcal{B}}_{j_2}\mathcal{B}_{j_1} + \mathcal{B}_{j_n}\cdots\mathcal{B}_{j_2}\tilde{\mathcal{B}}_{j_1}\Big)\mathcal{F}, \tag{A14a}$$

$$\mathcal{F}^{(n-1)}_{\boldsymbol{j}_r} \equiv \mathcal{B}_{j_n}\cdots\mathcal{B}_{j_{r+1}}\mathcal{B}_{j_{r-1}}\cdots\mathcal{B}_{j_1}\mathcal{F}, \tag{A14b}$$

$$\mathcal{F}^{(n+1)}_{\boldsymbol{j}j} \equiv \mathcal{B}_{j}\mathcal{B}_{j_n}\cdots\mathcal{B}_{j_1}\mathcal{F}, \tag{A14c}$$

where $\tilde{\mathcal{B}}_j \equiv \tilde{\mathcal{B}}^{\sigma}_{\alpha us} = -\mathrm{i}[\tilde{B}^{\sigma}_{\alpha us} - \tilde{B}'^{\sigma}_{\alpha us}]$ and

$$\tilde{B}^{\sigma}_{\alpha us} \equiv \sum_{us}\int_{t_0}^{t} \mathrm{d}\tau \dot{C}^{\sigma}_{\alpha uvs}(t,\tau) d^{\sigma}_{us}[\psi(\tau)]. \tag{A15}$$

We can derive a set of equations of motion about the influence functional and auxiliary influence functionals $\left\{\mathcal{F}^{(n)}_{\boldsymbol{j}} = \mathcal{F}^{(n)}_{j_1\cdots j_n}\right\}$ as

$$\partial_t \mathcal{F}^{(n)}_{\boldsymbol{j}} = \tilde{\mathcal{F}}^{(n)}_{\boldsymbol{j}} - \mathrm{i}\sum_{j}{}' \mathcal{A}_{\bar{j}}\mathcal{F}^{(n+1)}_{\boldsymbol{j}j} - \mathrm{i}\sum_{r=1}^{n}(-)^{(n-r)}\tilde{\mathcal{C}}_{j_r}\mathcal{F}^{(n-1)}_{j_r}, \tag{A16}$$

where

$$\tilde{\mathcal{C}}^{\sigma}_{\alpha us} = \sum_{us}\left\{C^{0,\sigma}_{\alpha uvs} d^{\sigma}_{v}[\psi[t]] - C^{0,\bar{\sigma}}_{\alpha uvs} d^{\sigma}_{us}[\psi'(t)]\right\}, \tag{A17}$$

with $C^{0,\sigma}_{\alpha uvs} \equiv C^{\sigma}_{\alpha uvs}(0) = C^{\sigma *}_{\alpha uvs}(0)$.

The auxiliary density operators (ADOs) $\left\{\rho^{(n)}_{\boldsymbol{j}} = \rho^{(n)}_{j_1\cdots j_n}\right\}$ are determined by the auxiliary influence functionals, like Eqs. (A1) and (A2),

$$\rho^{(n)}_{\boldsymbol{j}}(t) \equiv \mathcal{G}^{(n)}_{\boldsymbol{j}}(t,t_0)\rho(t_0), \tag{A18}$$

with propagators

$$\mathcal{G}^{(n)}_{\boldsymbol{j}}(\psi,t;\psi_0,t_0) \equiv \int_{\psi_0[t_0]}^{\psi[t]} \mathcal{D}\psi\, \mathrm{e}^{\mathrm{i}\mathcal{S}[\psi]}\mathcal{F}^{(n)}_{\boldsymbol{j}}[\psi]\,\mathrm{e}^{\mathrm{i}\mathcal{S}[\psi']}. \tag{A19}$$

Base on Eq. (A16) and Padé spectrum decomposition scheme, the final form can be reduced to the following compact form:

$$\dot{\rho}^{(n)}_{\boldsymbol{j}} = -\Big(\mathrm{i}\mathcal{L} + \sum_{r=1}^{n}\gamma_{j_r}\Big)\rho^{(n)}_{\boldsymbol{j}} - \mathrm{i}\sum_{j}\mathcal{A}_{\bar{j}}\rho^{(n+1)}_{\boldsymbol{j}j} - \mathrm{i}\sum_{r=1}^{n}(-)^{n-r}\mathcal{C}_{j_r}\rho^{(n-1)}_{\boldsymbol{j}_r}, \tag{A20}$$

in this expression, the index $\sigma = +/-$ in $j = \{\alpha us\sigma\}$ or $j = \{us\sigma\}$ corresponds to the transfer of an electron to/from the QD system; and the Grassmannian superoperators $\mathcal{A}_{\bar{j}} \equiv \mathcal{A}^{\bar{\sigma}}_{us}$ and $\mathcal{C}_j \equiv \mathcal{C}^{\sigma}_{uvsm}$ are defined via their fermionic actions on an operator $\hat{O}$ as $\mathcal{A}_j\hat{O} \equiv [\hat{d}^{\bar{\sigma}}_{us}, \hat{O}]$ and $\mathcal{C}_j\hat{O} \equiv \eta_j\hat{d}^{\sigma}_{us}\hat{O} + \eta^{*}_j\hat{O}\hat{d}^{\sigma}_{us}$, respectively. The on-dot electron interactions are contained in the Liouvillian of impurities, $\mathcal{L}\cdot \equiv [H_{\mathrm{sys}}, \cdot]$.

The transient current through the electrode α is

$$I_{\alpha}(t) = \mathrm{i}\sum_{\mu}\mathrm{tr}_{\mathrm{sys}}[\rho^{\dagger}_{\alpha\mu}(t)\hat{d}_{\mu} - \hat{d}^{\dagger}_{\mu}\rho^{-}_{\alpha\mu}(t)], \tag{A21}$$

where $\rho^{\dagger}_{\alpha\mu} = (\rho^{-}_{\alpha\mu})^{\dagger}$ is the first-tier auxiliary density operator obtained by solving Eq. (A20), and $\hat{d}_{\mu}$ ($\hat{d}^{\dagger}_{\mu}$) is the annihilation (creation) operator of an electron in the system marked by μ.

The details of the HEOM formalism can be found in Refs. [33,46,47]. Here, we focus on some of the key features of the formalism.

In formal, the HEOM formalism, Eq. (A20), is formally exact for arbitrary Fermion reservoirs satisfying Gaussian statistics,[33,48,49] and Eq. (A20) is nonperturbative.[51] Moreover, HEOM evaluations of system spectral density and transport current have been well-established.[4,33,46,50]

In numerical, via the approximation of an optimal Padé spectrum decomposition scheme,[52,53] the HEOM evaluation is practical with a converged truncation tier level at $L \equiv n_{\mathrm{trun}}$;

and $L=4$ is found to be enough in this work.

In recent works, the HEOM method has been shown to be capable in a wide range of applications including description of the Kondo effect. For example, Li *et al.* showed that this approach can quantitatively describe the Kondo resonance and Fermi-liquid characteristics.[4] In a time-dependent view, Cheng *et al.* investigated transport properties of single and double quantum impurity systems with Kondo resonance.[54] Pan *et al.* studied the Kondo effect in the context of ferromagnetic RKKY interaction.[55] Ye *et al.* applied the HEOM approach on two-level QDs with Kondo correlations, providing an understanding of, and a viable mechanism for controlling, the thermoelectric properties of strongly correlated QD systems.[56] Finally, in open triple QDs, Cheng *et al.* investigated the reappearance of the Kondo effect and long-range overlapping of Kondo clouds via the HEOM approach.[57,58]

Appendix B: Numerical Green's function

In the present paper, both numerical and analytical methods involve Green's function. For the dynamical quantities, we start with the reduced density matrix in the HEOM linear space, which writes

$$\boldsymbol{\rho}(t)\equiv\left\{\rho(t),\rho_{\boldsymbol{j}}^{(n)}(t);n=1,2,...,L\right\},\tag{B1}$$

the time evolution of $\boldsymbol{\rho}(t)$ is

$$\boldsymbol{\rho}(t)=\mathcal{G}(t,t_0)\boldsymbol{\rho}(t_0).\tag{B2}$$

For an arbitrary operator of the QD system in the HEOM linear space, we have

$$\boldsymbol{A}(t)\equiv\left\{A,A_{\boldsymbol{j}}^{(n)};n=1,2,\ldots,L\right\},\tag{B3}$$

where A is an ordinary physical operator and $\left\{A_{\boldsymbol{j}}^{(n)};n=1,2,\ldots,L\right\}$ is the corresponding auxiliary part, and

$$\boldsymbol{A}(t)=\boldsymbol{A}(t_0)\mathcal{G}(t,t_0);\ \boldsymbol{A}(t_0)=\{A,\boldsymbol{0}\}.\tag{B4}$$

The definition of inner product for two arbitrary operators in the HEOM linear space writes

$$\langle\langle\boldsymbol{A}|\boldsymbol{B}\rangle\rangle\equiv\langle\langle A|B\rangle\rangle+\sum_{n=1}^{N}\left\langle\left\langle A_j^{(n)}|B_j^{(n)}\right\rangle\right\rangle,\tag{B5}$$

where $\langle\langle A|B\rangle\rangle=\mathrm{Tr}[A^{+}B]$ and $\langle\langle A_j^{(n)}|B_j^{(n)}\rangle\rangle=\mathrm{Tr}\left[{A_j^{(n)}}^{+}B_j^{(n)}\right]$.

The correlation function for two arbitrary operators of the system in the Heisenberg picture writes

$$\widetilde{C}_{AB}(t)\equiv\langle\langle\boldsymbol{A}(t)|\boldsymbol{B}\boldsymbol{\rho}_{\mathrm{eq}}(T)\rangle\rangle,\tag{B6}$$

where $\boldsymbol{\rho}_{\mathrm{eq}}(T)=\left\{\rho_{\mathrm{eq}},\rho_{\mathrm{eq}}^{(n)};n=1,2,\ldots,N\right\}$ is the reduced density matrix of thermal equilibrium state, and $\boldsymbol{B}\boldsymbol{\rho}_{\mathrm{eq}}(T)=\left\{B\rho_{\mathrm{eq}},B\rho_{\mathrm{eq}}^{(n)};n=1,2,\ldots,N\right\}$ can be regarded as an operator in HEOM space.

HEOM numerical evaluation focuses on the reduced system density [cf. Eq. (A20)], including the influence of environment at every tier; thus, we are able to retrieve $\widetilde{C}_{AB}(t)$ exactly. By taking the Fourier transform $C_{AB}(\omega)\equiv\frac{1}{2}\int\mathrm{d}t\,\mathrm{e}^{\mathrm{i}\omega t}\widetilde{C}_{AB}(t)$, $C_{AB}(-\omega)=\mathrm{e}^{-\omega/k_{\mathrm{B}}T}C_{AB}(\omega)$, we are able to obtain the correlation function in the frequency domain. Let $\hat{A}=\hat{d}_\mu$ and $\hat{B}=\hat{d}_\mu^{\dagger}$. In this case the correlation function is reduced into the Green's function $G_{\mu\mu}(\omega)=C_{\hat{d}_\mu\hat{d}_\mu^{\dagger}}(\omega)$.

In this context, we care about the retarded Green's function and the spectral function of QD1, so that $\hat{d}_\mu(\hat{d}_\mu^{\dagger})=\hat{d}_{1s}(\hat{d}_{1s}^{\dagger})$. For the degeneracy of spin, we have $G(\omega)=G_{1\uparrow}(\omega)=G_{1\downarrow}(\omega)$ for simplicity. The corresponding spectral function is

$$A(\omega)=-\frac{1}{\pi}\mathrm{Im}G(\omega).\tag{B7}$$

Appendix C: Analytical Green's function for background

Analytically, we can derive the Green's function for an isolated DQD described by Eq. (1)

$$\begin{aligned}G_{us,us}^{\mathrm{iso}}(\omega)=&\frac{1-\langle\hat{n}_{u\bar{s}}\rangle-\langle\hat{n}_{vs}\rangle-\langle\hat{n}_{v\bar{s}}\rangle+\langle\hat{n}_{u\bar{s}}\hat{n}_{vs}\rangle+\langle\hat{n}_{u\bar{s}}\hat{n}_{v\bar{s}}\rangle+\langle\hat{n}_{vs}\hat{n}_{v\bar{s}}\rangle-\langle\hat{n}_{u\bar{s}}\hat{n}_{vs}\hat{n}_{v\bar{s}}\rangle}{\omega-\epsilon_d+\mathrm{i}\zeta}\\&+\frac{\langle\hat{n}_{u\bar{s}}\rangle-\langle\hat{n}_{u\bar{s}}\hat{n}_{vs}\rangle-\langle\hat{n}_{u\bar{s}}\hat{n}_{v\bar{s}}\rangle+\langle\hat{n}_{u\bar{s}}\hat{n}_{vs}\hat{n}_{v\bar{s}}\rangle}{\omega-\epsilon_d-U+\mathrm{i}\zeta}\\&+\frac{\langle\hat{n}_{vs}\rangle+\langle\hat{n}_{v\bar{s}}\rangle-\langle\hat{n}_{u\bar{s}}\hat{n}_{vs}\rangle-\langle\hat{n}_{u\bar{s}}\hat{n}_{v\bar{s}}\rangle-2\langle\hat{n}_{vs}\hat{n}_{v\bar{s}}\rangle+2\langle\hat{n}_{u\bar{s}}\hat{n}_{vs}\hat{n}_{v\bar{s}}\rangle}{\omega-\epsilon_d-U_{12}+\mathrm{i}\zeta}\\&+\frac{\langle\hat{n}_{u\bar{s}}\hat{n}_{vs}\rangle+\langle\hat{n}_{u\bar{s}}\hat{n}_{v\bar{s}}\rangle-2\langle\hat{n}_{u\bar{s}}\hat{n}_{vs}\hat{n}_{v\bar{s}}\rangle}{\omega-\epsilon_d-U_{12}-U+\mathrm{i}\zeta}+\frac{\langle\hat{n}_{vs}\hat{n}_{v\bar{s}}\rangle-\langle\hat{n}_{u\bar{s}}\hat{n}_{vs}\hat{n}_{v\bar{s}}\rangle}{\omega-\epsilon_d-2U_{12}+\mathrm{i}\zeta}+\frac{\langle\hat{n}_{u\bar{s}}\hat{n}_{vs}\hat{n}_{v\bar{s}}\rangle}{\omega-\epsilon_d-2U_{12}-U+\mathrm{i}\zeta},\end{aligned}\tag{C1}$$

where $\zeta=0^{+}$ comes from the decay factor $\mathrm{e}^{-\zeta t}$ for convergence of the Fourier transform, with $u\neq v$ and $u,v=1,2$ marking QD1 and QD2. Without any connection to the environment, QDs in the isolated DQD are equal. Taking our capacitive side-coupling configuration (cf. Fig. 1) into consideration, we focus on QD1, despite of spin index for its degeneracy, let $u=1$ and $v=2$, then we obtain the Green's function of QD1 in the isolated DQD and abbreviate it as

$$G^{\mathrm{iso}}(\omega)=G_{us,us}^{\mathrm{iso}}(\omega)\,|_{u=1,s=\uparrow\text{ or }\downarrow}.\tag{C2}$$

A pole in a retarded Green's function indicates an elementary excitation. There are six poles in Eq. (C1); in each

pole term, the numerator indicates the weight of an elementary excitation, while the denominator denotes its position. This means the six substates are at $\omega = \epsilon_d$, $\epsilon_d + U$, $\epsilon_d + U_{12}$, $\epsilon_d + U_{12} + U$, $\epsilon_d + 2U_{12}$, and $\epsilon_d + 2U_{12} + U$.

We start with $U_{12} = 0$. The side-coupled DQD is reduced to a single QD since QD2 is completely isolated. The six poles mentioned above degenerate into two at $\omega = \epsilon_d$ and $\epsilon_d + U$; these poles are Hubbard resonances called the singly-occupied (S-O) state and the doubly-occupied (D-O) state. The S-O and D-O states describe the excitations $|0\rangle \to |1\rangle$ and $|1\rangle \to |2\rangle$ for a single dot, respectively. When $U_{12} > 0$, the S-O (D-O) state generates three S-O (D-O) substates at $\omega = \epsilon_d + mU_{12}(+U)$, $(m = 0, 1, 2)$. We label these S-O (D-O) substates as S-O_0, S-O_1, S-O_2 (D-O_0, D-O_1, D-O_2) states (cf. Fig. 1).

Via mean-field approach, which sets $\langle \hat{n}_\mu \hat{n}_{\mu'} \rangle = \langle \hat{n}_\mu \rangle \langle \hat{n}_{\mu'} \rangle$, $\langle \hat{n}_\mu \hat{n}_{\mu'} \hat{n}_{\mu''} \rangle = \langle \hat{n}_\mu \rangle \langle \hat{n}_\mu \rangle \langle \hat{n}_{\mu''} \rangle$, and takes $\zeta = 0.4$ meV, we find that the result perfectly matches the numerical result from HEOM at 2 meV for temperature and at 0.2 meV for hybridization.

Acknowledgments

We would like to thank Zhen-Gang Zhu for the valuable discussions.

References

[1] Kondo J 1964 *Prog. Theor. Phys.* **32** 37
[2] Costi T A, Hewson A C and Zlatić 1994 *J. Phys.: Condens. Matter* **6** 2519
[3] Hewson A C 1993 *The Kondo Problem to Heavy Fermions* (Cambridge: Cambridge University Press) pp. 47–65
[4] Li Z H, Tong N H, Zheng X, Hou D, Wei J H, Hu J and Yan Y J 2012 *Phys. Rev. Lett.* **109** 266403
[5] Li J, Schneider W D, Berndt R and Delley B 1998 *Phys. Rev. Lett.* **80** 2893
[6] Göres J, Goldhaber-Gordon D, Heemeyer S, Kastner M A, Shtrikman H, Mahalu D and Meirav U 2000 *Phys. Rev. B* **62** 2188
[7] Zacharia I G, Goldhaber-Gordon D, Granger G, Kastner M A, Khavin Y B, Shtrikman H, Mahalu D and Meirav U 2001 *Phys. Rev. B* **64** 155311
[8] Sasaki S, Tamura H, Akazaki T and Fujisawa T 2009 *Phys. Rev. Lett.* **103** 266806
[9] Žitko R 2010 *Phys. Rev. B* **81** 115316
[10] Oreg Y and Goldhaber-Gordon D 2003 *Phys. Rev. Lett.* **90** 136602
[11] Lebanon E, Schiller A and Anders F B 2003 *Phys. Rev. B* **68** 155301
[12] Cornaglia P S and Grempel D R 2005 *Phys. Rev. B* **71** 075305
[13] Žitko R and Bonča J 2006 *Phys. Rev. B* **73** 035332
[14] Žitko R and Bonča J 2007 *J. Phys.: Condens. Matter* **19** 255205
[15] Chung C H, Zarand G and Wölfle P 2008 *Phys. Rev. B* **77** 035120
[16] Chung C H and Lee T H 2010 *Phys. Rev. B* **82** 085325
[17] Tanaka Y, Kawakami N and Oguri A2012 *Phys. Rev. B* **85** 155314
[18] Andrade J A, Cornaglia P S and Aligia A A 2014 *Phys. Rev. B* **89** 115110
[19] Chan I H, Westervelt R M, Maranowski K D and Gossard A C 2002 *Appl. Phys. Lett.* **80** 1818
[20] Chan I H, Fallahi P, Westervelt R M, Maranowski K D and Gossard A C 2003 *Physica E* **17** 584
[21] Holleitner A W, Blick R H and Eberl K 2003 *Appl. Phys. Lett.* **82** 1887
[22] McClure D T, DiCarlo L, Zhang Y, Engel H A, Marcus C M, Hanson M P and Gossard A C 2007 *Phys. Rev. Lett.* **98** 056801
[23] Hübel A, Weis J, Dietsche W and Klitzing K v 2007 *Appl. Phys. Lett.* **91** 102101
[24] Hübel A, Held K, Weis J and Klitzing K v 2008 *Phys. Rev. Lett.* **101** 186804
[25] Okazaki Y, Sasaki S and Muraki K 2011 *Phys. Rev. B* **84** 161305
[26] López R, Aguado R and Platero G 2002 *Phys. Rev. Lett.* **89** 136802
[27] Mravlje J, Ramsak A and Rejec T 2006 *Phys. Rev. B.* **73** 241305
[28] Lipinski S and Krychowski D 2007 *J. Magn. Magn. Mater.* **310** 2423
[29] Hatano T, Amaha S, Kubo T, Teraoka S, Tokura Y, Gupta J A, Austing D G and Tarucha S 2010 *Appl. Phys. Lett.* **97** 062108
[30] Ruiz–Tijerina D A, Vernek E and Ulloa S E 2014 *Phys. Rev. B* **90** 035119
[31] Galpin M R, Logan D E and Krishnamurthy H R 2005 *Phys. Rev. Lett.* **94**186406
[32] Krychowski D, Florkow P, Antkiewicz M and Lipinski S 2018 *Phys. E* **98** 74
[33] Jin J S, Zheng X and Yan Y J 2008 *J. Chem. Phys.* **128** 234703
[34] Camacho G, Schmitteckert P and Carr S T 2019 *Phys. Rev. B* **99** 085122
[35] Luo H G, Xiang T, Wang X Q, Su Z B and Yu L 2004 *Phys. Rev. Lett.* **92** 256602
[36] Luo H G, Xiang T, Wang X Q, Su Z B and Yu L 2006 *Phys. Rev. Lett.* **96** 019702
[37] Wei J H and Yan Y J 2011 *arXiv:1108.5955*
[38] Li Z H, Cheng Y X, Wei J H, Zheng X and Yan Y J 2018 *Phys. Rev. B* **98** 115133
[39] Fano U 1961 *Phys. Rev.* **124** 1866
[40] Miroshnichenko A E, Flach S and Kivshar Y S 2010 *Rev. Mod. Phys.* **82** 2257
[41] Hobvtić B and Zlatić V 1980 *Phys. Status. Solidi. B* **99** 251
[42] Feynman R P and Vernon, Jr. F L 1963 *Ann. Phys.* **24** 118
[43] Kleinert H 2009 *Path Integrals in Quantum Mechanics, Statistics, Polymer Physics, and Financial Markets*, 5th edn. (Singapore: World Scientific) pp. 654–663
[44] Xu R X, Cui P, Li X Q, Mo Y and Yan Y J 2005 *J. Chem. Phys.* **122** 041103
[45] Xu R X and Yan Y J 2007 *Phys. Rev. E* **75** 031107
[46] Zheng X, Jin J S, Welack S, Luo M and Yan Y J 2009 *J. Chem. Phys.* **130** 164708
[47] Zheng X, Xu R X, Xu J, Jin J S, Hu J and Yan Y J 2012 *Prog. Chem.* **24** 1129
[48] Yan Y J 2014 *J. Chem. Phys.* **140** 054105
[49] Yan Y J, Jin J S, Xu R X and Zheng X 2016 *Frontiers Phys.* **11** 110306
[50] Zheng X, Yan Y J, Di Ventra M 2013 *Phys. Rev. Lett.* **111** 086601
[51] Han L, Zhang H D, Zheng X and Yan Y J 2018 *J. Phys. Chem.* **148** 234108
[52] Hu J, Xu R X and Yan Y J 2010 *J. Chem. Phys.* **133** 101106
[53] Hu J, Luo M, Jiang F, Xu R X and Yan Y J 2011 *J. Chem. Phys.* **134** 244106
[54] Cheng Y X, Hou W J, Wang Y D, Li Z H, Wei J H and Yan Y J 2015 *New J. Phys.* **17** 033009
[55] Pan L, Wang Y D, Li Z H, Wei J H and Yan Y J 2017 *J. Phys.: Condens. Matter* **29** 025601
[56] Ye L Z, Hou D, Wang R L, Cao D W, Zheng X and Yan Y J 2014 *Phys. Rev. B* **90** 165116
[57] Cheng Y X, Wei J H and Yan Y J 2015 *EPL* **112** 57001
[58] Cheng Y X, Wang Y D, Wei J H, Luo H G and Lin H Q 2019 *J. Phys.: Condens. Matter* **31** 155302